Offline Bayesian Change Point Detection for Carrier-Phase in GNSS-Reflectometry

1st Ali Chamseddine
LISIC Laboratory
Université du Littoral Côte d'Opale
Calais, France
ali.chamseddine@etu.univ-littoral.fr

2nd Georges Stienne
LISIC Laboratory
Université du Littoral Côte d'Opale
Calais, France
georges.stienne@univ-littoral.fr

3rd Serge Reboul
LISIC Laboratory
Université du Littoral Côte d'Opale
Calais, France
serge.reboul@univ-littoral.fr

4th Ghaleb Faour
Remote Sensing Center
CNRS-Lebanon
Beirut, Lebanon
gfaour@cnrs.edu.lb

***Abstract*—Change detection techniques are essential for identifying and quantifying variations in data over time, with applications in remote sensing, signal processing, and environmental monitoring. The ability of GNSS-Reflectometry (GNSS-R), a bistatic radar technique that utilizes navigation satellite signals as signals of opportunity, to analyze surface characteristics has recently been explored by studying the coherence of reflected GNSS signal phases. However, detecting changes in the carrier phase of multiple reflections GNSS signals remains unexplored in the literature, as conventional change detection methods are designed for linear data, whereas phase data is inherently circular. In this work, we adapt an offline Bayesian Change-Point Detection approach, assuming the phase noise follows a Von Mises distribution, to detect changes in the reflected GNSS signal by estimating change points through minimizing a contrast function. The method is evaluated using both synthetic and real GNSS-R measurements, demonstrating superior performance compared to a conventional spectral change detection technique. Results highlight the method's accuracy in detecting surface variations in real GNSS-R observations.**

***Index Terms*—Phase Coherence, Remote Sensing, Change Detection, GNSS-Reflectometry**

I. Introduction

GNSS-Reflectometry (GNSS-R) is an advanced remote sensing technique derived from GNSS technology. It utilizes continuously available GNSS signals reflected on Earth's surface, functioning as a passive bistatic radar. Since GNSS-R does not require a dedicated signal transmitter, it offers a cost-effective solution for remote sensing. Additionally, this method provides extensive coverage and high spatial resolution, as a GNSS receiver can simultaneously process signals from multiple satellites. In the case of spaceborne GNSS-R measurements, ground reflection tracks can span several hundred kilometers apart [1]. However, in this work, where airborne GNSS-R measurements are used at an average altitude of 315m and an average speed of 95km/h, sub-meter spatial resolution can be reached.

The authors would like to thank the CPER IDEAL (approche Intégrée des Défis mAritimes et Littoraux) program for their financial support.

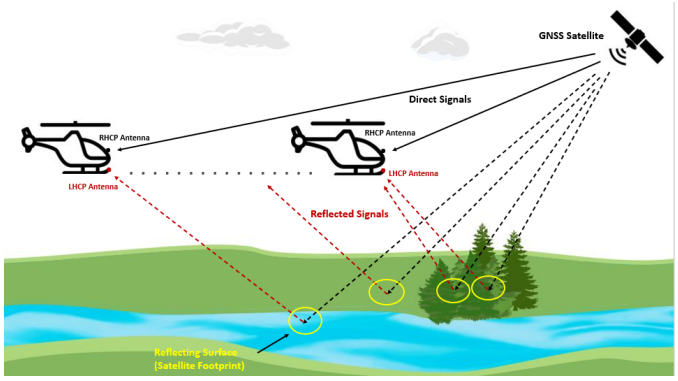

Fig. 1: GNSS-R phase coherence concept.

The phase coherence of the reflected GNSS carrier signal is influenced by surface deformation and roughness, with smoother and less deformed areas scattering the signal more coherently [2]. As shown in Fig 1, when multiple reflections of a GNSS signal come from a rough surface and reach a GNSS-R sensor, the measured signal becomes non-coherent, impacting all processed parameters, including amplitude, carrier frequency, and carrier phase over time. In such cases, temporal phase coherence is lost as the geometry between the GNSS satellite, the reflecting surface, and the GNSS-R receiver changes over time.

In a previous work [3], the Rayleigh Test (RT) of uniformity has been explored for detecting changes in carrier-phase coherence, demonstrating that RT provides highly contrasted outputs, particularly in oscillatory phase data. While [4] demonstrates that under uniformity, the RT statistic follows a known χ^2_2 distribution, its distribution under non-uniformity requires a more general characterization. For this reason, in this work, we apply our change detection approach directly

to the carrier phase, considering that the GNSS carrier phase noise follows a Von Mises distribution.

Offline change-point detection methods are used for optimal signal segmentation. These approaches typically rely on the assumption that the signal's statistical properties are known [5]. In this work, the phase data noise is assumed to follow a Von Mises distribution. In [6], a Bayesian estimation method was introduced for the joint segmentation of piecewise stationary processes. Here, we adapt the approach from [6] to the phase of reflected GNSS signals as a univariate change detection method. In Bayesian analysis, assigning probability distributions to both the change points and the parameters is essential [7]. In this study, we estimate the phase of the reflected signal by first determining the signal's parameters through the spectral representation of the excess Doppler, which is derived from the phase evolution in an open-loop tracking configuration of a bi-static system. Subsequently, we apply offline Bayesian Change-Point Detection to identify the moments of change in these values. Spectral change detection methods have been widely explored for analyzing spectral variations in various applications. In [8] the authors propose an unsupervised change detection (CD) method for remote sensing that can handle large differences in spatial resolution and spectral bands between pre-change and post-change images. In [9] an approach for spectral alignment of multi-temporal cross-sensor remote sensing images was proposed using kernel canonical correlation analysis (kCCA), the method projects images from different and potentially disjoint spectral spaces into a common latent space, enabling the application of standard change detection algorithms while automatically selecting model parameters to optimize alignment and feature extraction. [10] and [11] have introduced a change detection method based on spectral variations using Euclidean Distance. In this paper, we will compare our approach with this spectral change detection method that utilizes Euclidean Distance (ED).

This paper is structured as follows: Section 2 introduces the phase model of the GNSS reflected signal. Section 3 provides the derivation of the equations for estimating the parameters. Section 4 presents the results and analysis of an experiment conducted with synthetic data, and also in section 4 demonstrates the application of our method to real GNSS-R measurement data. Finally, Section 5 concludes the paper.

II. Phase Model

The change detection approach will be applied on the phase of the reflected GNSS signal. Let consider the following reflected GNSS signal:

$$s_r(t) = \sum_{u=1}^{U} a_u CA(t + \tau_u^r) \sin(2\pi f_1 t + \Phi_u(t)) + \eta(t) \quad (1)$$

where $\eta(t)$ is a Gaussian noise. $CA(\dots)$ the CDMA code of the GNSS signal is defined as $CA(\dots) \in \{-1, 1\}$. This modelization assume that we have R reflections with different Doppler (so different phase errors) and amplitudes. The carrier phase is estimated using a Locked Loop for the direct signal and an Open Loop for the reflected signal as mentioned in [12]. We show that the two components in quadrature provided by the Open Loop every period of CDMA code T_c can be modeled as follows:

$$I_i = \sum_{u=1}^{U} A_u \ \cos(\alpha_u + \phi_u i) + \eta_I(i) \quad (2)$$

$$Q_i = \sum_{u=1}^{U} A_u \ \sin(\alpha_u + \phi_u i) + \eta_Q(i) \quad (3)$$

where $i \in \{T_c, \dots, N * T_c\}$. $\eta_I(i), \eta_Q(i)$ are Gaussian noises. $\phi_u = 2\pi f d_u$ with $f d_u$ the excess Doppler associated to the u^{th} reflection. The observed reflected phase can be modeled as:

$$y_i = \arctan\left(\frac{Q_i}{I_i}\right) = \lfloor \bar{y}_i + \xi_i \rfloor \mod 2\pi \quad (4)$$

where the phase $\bar{y}_i$ is the weighted sum of the phases $\{\alpha_u + \phi_u i\}_{u=1,\dots,U}$ in the circular domain and $\{A_u\}_{u=1,\dots,U}$ are the weights [13]. ξ_i is an additive noise distributed according to a centered Von Mises distribution.

We consider the following likelihood for several reflections:

$$f(y_i; \alpha_u, A_u, \phi_u, \kappa) = \frac{1}{2\pi I_0(\kappa)} \exp\left(\kappa \cos\left(y_i - \bar{y}_i\right)\right) \quad (5)$$

where κ is the concentration parameter of the Von Mises distribution. I_0 is the modified Bessel function of the first kind and order zero.

III. Bayesian Estimation for Change Detection

In our Bayesian change detection approach, Let $\underline{y} = (y_i, 1 \le i \le n)$ be the phase data. We assume that the process is piecewise stationary. Let $\underline{r} = (r_i, 1 \le i \le n)$ be the configuration of change points in the process $\underline{y}$. Let $\hat{t} = (t_k, k \ge 0, t_0 = 0)$ be the real instant of change we want to detect. The value of r_i is 0 between two changes and 1 at the change instant. Let $\underline{\theta} = (\theta_1, \dots, \theta_K)$ be the sequence of parameters in the process y, composed of k stationary segments (θ_k is the parameter in the k-th segment of the series $\underline{y}$).

The parameters $\underline{\theta}$ and the sequence of changes $\underline{r}$ are estimated by maximizing the posterior distribution:

$$(\hat{\underline{r}}, \hat{\underline{\theta}}) = \arg\max_{(\underline{r}, \underline{\theta})} Pr(R = \underline{r} \mid Y = \underline{y}; \underline{\theta}) \quad (6)$$

$$(\hat{\underline{r}}, \hat{\underline{\theta}}) = \arg\max_{(\underline{r}, \underline{\theta})} h(\underline{y} \mid \underline{r}, \underline{\theta}) f(\underline{\theta}) p(\underline{r}) \quad (7)$$

where $p(\underline{r})$, the prior law of $\underline{r}$, is given by:

$$p(\underline{r}) = \lambda^K (1 - \lambda)^{n-K}, \quad (8)$$

with λ the probability of a change on $\underline{y}$ and

$$K = \sum_{i=1}^{n} r_i + 1,$$

Let $f(\underline{\theta})$ be the probability to have the sequence of parameters θ for the process $\underline{y}$. We do not have any prior information on $\underline{y}$, so we suppose $f(\theta)$ to follow a uniform distribution. In our approach the parameters $\underline{\theta}$ are estimated as $\hat{\underline{\theta}}$. When we take the negative logarithm of Eq. (5), we define a penalized empirical criterion, where $\underline{r}$ (the number and position of changes) is estimated by minimizing the penalized contrast function defined by:

$$U_y(\hat{\underline{r}}) = V_y(\hat{\underline{r}}, \hat{\underline{\theta}}(\hat{\underline{r}})) - \ln p(\hat{\underline{r}}) \tag{9}$$

The parameter λ of the penalization is fixed by the user.

IV. Parameters Estimation

$\hat{\underline{\theta}}(\hat{\underline{r}})$ is the parameter vector including $\left\{\hat{\alpha}_{u,k}, \hat{\phi}_{u,k}, \hat{A}_{u,k}\right\}_{u=1,\ldots,U}$, and $\hat{\kappa}_k$ is estimated for each segment k. The excess Doppler spectrum is given by $\Gamma(f) = TF(I_n + jQ_n)$. The expression of the norm of the spectrum is:

$$|\Gamma(f)| = \sum_{u=1}^{U} A_{u,k}\delta(f - \frac{\phi_{u,k}}{2\pi}) + \Psi \tag{10}$$

where $\delta(f)$ is the Dirac function, Ψ is a noise and $A_{u,k}$ is the power of the u^{th} reflection. We define $\left\{\hat{\phi}_{u,k}, \hat{A}_{u,k}\right\}$ respectively as the frequencies and amplitudes of the peaks in the spectrum $\Gamma(f)$. The phase $\alpha_{u,k}$ is estimated using the phase of the excess Doppler spectrum:

$$\hat{\alpha}_{u,k} = \angle\left(\Gamma(\frac{\hat{\phi}_{u,k}}{2\pi})\right) \tag{11}$$

We show in [13], that the maximum likelihood estimate $\hat{\kappa}_k$ is given by the following equation:

$$\hat{\kappa}_k = A^{-1}(\frac{1}{N}\sum_{n=t_{k-1}}^{t_k}\cos(y_n - \hat{y}_{k,n})) \tag{12}$$

$$\hat{y}_{k,n} = \arctan\left(\frac{\sum_{u=1}^{U}\hat{A}_{u,k}\ \sin(\hat{\alpha}_{u,k} + \hat{\phi}_{u,k}n)}{\sum_{u=1}^{U}\hat{A}_{u,k}\ \cos(\hat{\alpha}_{u,k} + \hat{\phi}_{u,k}n)}\right) \tag{13}$$

with $A(x) = \frac{I_1(x)}{I_0(x)}$. Finally, the contrast function can be processed with the following equation:

$$V_y(\hat{\underline{r}}, \hat{\underline{\theta}}(\hat{\underline{r}})) = \sum_{k=1}^{K}\left\{n_2 \log I_0(\hat{\kappa}_k) - \hat{\kappa}_k \sum_{n=t_{k-1}}^{t_k}\cos\left(y_n - \hat{y}_{k,n}\right)\right\} \tag{14}$$

V. Experimentation

A. Using Synthetic data

According to [11], the Euclidean Distance (ED) used to detect spectral changes, leading to the following mathematical formulation:

$$ED = \sum_{i=1}^{nb}(T_1^i - T_2^i)^2 \tag{15}$$

where T_1^i and T_2^i represent the spectral values and reference spectrum for the i-th feature, and nb is the total number of spectral bands. A lower Euclidean distance signifies a greater similarity between spectra, thereby indicating minimal change in the observed region. This method of reference is compared to the proposed approach.

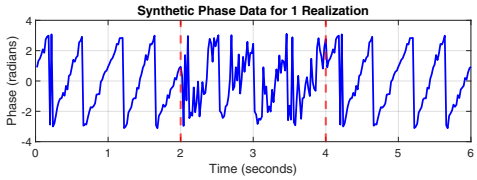

(a) Change Detection results for one realization of synthetic phase data

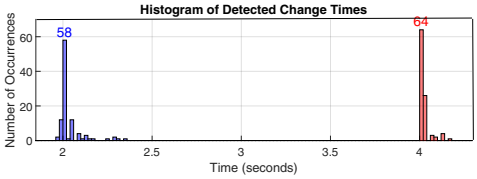

(b) Histogram of the change detection method using Euclidian Distance (ED): Distribution of detected changes over 100 realization.

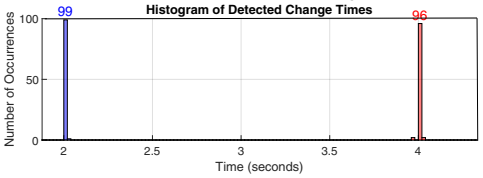

(c) Histogram of our proposed method's results: Distribution of detected changes over 100 realization.

Fig. 2: Comparison of change detection and probability of good detection for synthetic data: Evaluating the performance of the detection methods.

In order to evaluate the proposed change detection method, we simulated 6 seconds of GNSS signal phase data with two reflections, consisting of three distinct segments with two changes on y_1 at $t = 2$ seconds and y_2 at $t = 4$ seconds as shown in 2 (a). The first and the third segments represent the coherent phase and the second segment represents the non-coherent phase. The parameter vectors $\hat{\alpha}$, $\hat{\phi}$, $\hat{A}$ and $\hat{\kappa}$ for the three segments were estimated using the equations provided in Section 4. For the first and last 2 seconds, representing the coherent segments, the parameter estimates are computed in Table 1. For the second segment, the parameters estimated for the non-coherent phase are presented in Table 2.

TABLE I: Parameter estimates for Figure 2 (a), first and last segments (coherent).

Parameter	Estimated Values
$\hat{\phi}$	12.56, 6.28
$\hat{\alpha}$	1.14, 1.35
$\hat{A}$ ($\times 10^6$)	3.17, 0.90
$\hat{\kappa}$	19.19

TABLE II: Parameter estimates for Figure 2 (a), second segment (non-coherent).

Parameter	Estimated Values
$\hat{\phi}$	12.56, 65.97
$\hat{\alpha}$	3.01, 2.37
$\hat{A}$ ($\times 10^6$)	3.16, 0.96
$\hat{\kappa}$	1.45

By minimizing Equation (13), the change point, $\hat{r}$, was accurately identified at $t = 2$ and $t = 4$ seconds. The multiple search method for this change detection approach is implemented as described in [6].

Figure 2 (b) and (c) presents the histograms of detected changes across 100 realizations for the methods proposed in [10] and [11], as well as for our proposed method. In our method, the true changes at $t = 2$ s and $t = 4$ s were successfully detected in 99 and 96 out of 100 realizations, corresponding to detection probabilities of 0.99 and 0.96, respectively. In contrast, when using the Euclidean Distance method from [10] and [11], the detection probabilities for $t = 2$ s and $t = 4$ s were only 0.58 and 0.64, respectively. This demonstrates that our proposed method significantly outperforms the spectral change detection approach based on Euclidean Distance in detecting changes.

B. Using Real GNSS-R measurement

The experimental data used in this study were collected in the northern region of France on October 19, 2020, at 14:45 UTC [14]. The GNSS-R receiver consisted of an up-looking RHCP antenna, a down-looking LHCP antenna, and a fiber optic coil that enabled the synchronous digitization of both the LCHP and RHCP signals (see [14]), using a Syntony GNSS L1-L5 mono-channel bit grabber with a 25 MHz sampling rate. This equipment was mounted on a gyrocopter. The flight duration was 45 minutes, with an average altitude of 315 meters and a speed of 95 km/h. The change detection process was realized using the recorded GPS L1 signals.

Figure 3 displays 15 seconds of phase data from the reflected GNSS signal of GPS satellite PRN 5, divided into two segments. The first segment corresponds to a lake, which is a very smooth surface , while the second segment represents land (considered a rough surface). Figure 4 displays 10 seconds of phase data from the reflected GNSS signal of GPS satellite PRN 5, divided into two segments, the first segment represents the land, while the second segment corresponds a smooth lake surface.
The parameter estimates for the first segment in Figure 3 represent the coherent segment. The estimated values for $\hat{\phi}$, $\hat{\alpha}$, $\hat{A}$ and $\hat{\kappa}$ are provided in Table 3.

TABLE III: Parameter estimates for Figure 3, first segment (coherent).

Parameter	Estimated Values
$\hat{\phi}$	303.99, 300.14, 297.04
$\hat{\alpha}$	-1.24, -1.14, -1.48
$\hat{A}$ ($\times 10^5$)	2.67, 1.61, 0.89
$\hat{\kappa}$	3.84

TABLE IV: Parameter estimates for Figure 3, first segment (non-coherent).

Parameter	Estimated Values
$\hat{\phi}$	304.59, 295.09, 2.45, 0.12, 291.93, 6.11, 305.16, 284.11
$\hat{\alpha}$	0.96, -2.43, -1.12, 1.62, 0.31, 2.12, -1.58, 1.43
$\hat{A}$ ($\times 10^5$)	1.46, 1.41, 1.34, 1.31, 1.25, 1.24, 1.22, 1.19
$\hat{\kappa}$	0.49

The parameter estimates for the second segment in Figure 3 represent the non-coherent phase. The estimated values for $\hat{\phi}$, $\hat{\alpha}$, $\hat{A}$, and $\hat{\kappa}$ are provided in Table 4.

TABLE V: Parameter estimates for Figure 4, first segment (non-coherent).

Parameter	Estimated Values
$\hat{\phi}$	26.81, 305.59, 58.95, 243.73, 2.71, 66.40
$\hat{\alpha}$	1.64, 2.80, 0.16, 1.94, 1.03, 1.38
$\hat{A}$ ($\times 10^4$)	8.02, 7.83, 7.34, 6.71, 6.68, 6.58
$\hat{\kappa}$	0.52

The parameter estimates for the first segment in Figure 4 represent the non-coherent segment. The estimated values for $\hat{\phi}$, $\hat{\alpha}$, $\hat{A}$, and $\hat{\kappa}$ are provided in Table 5.

TABLE VI: Parameter estimates for Figure 4, first segment (coherent).

Parameter	Estimated Values
$\hat{\phi}$	9.23, 13.94, 17.57
$\hat{\alpha}$	0.41, 1.84, -0.54
$\hat{A}$ ($\times 10^4$)	25.72, 16.61, 7.54
$\hat{\kappa}$	3.04

Finally, for the second segment of Figure 4, which represents the coherent segment, the parameter estimates are shown

in Table 6. These estimates represent the behavior of the reflected signal in a coherent environment, with higher $\hat{\kappa}$ values indicating improved coherence. The estimated values for $\hat{\phi}$, $\hat{\alpha}$ and $\hat{A}$ highlight the distinct features between the non-coherent and coherent segments.

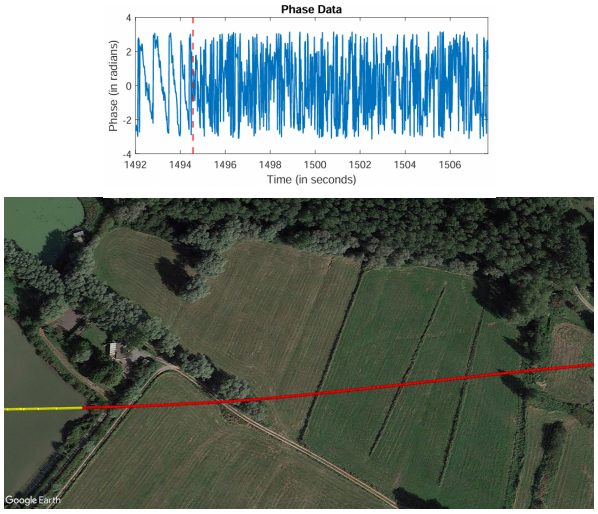

Fig. 3: 15 seconds of phase data from the reflected GNSS signal of GPS satellite PRN 5, representing a smooth lake surface(in yellow) in the first segment, and a rough land surface(in red) in the second segment, with the detected change accurately identified.

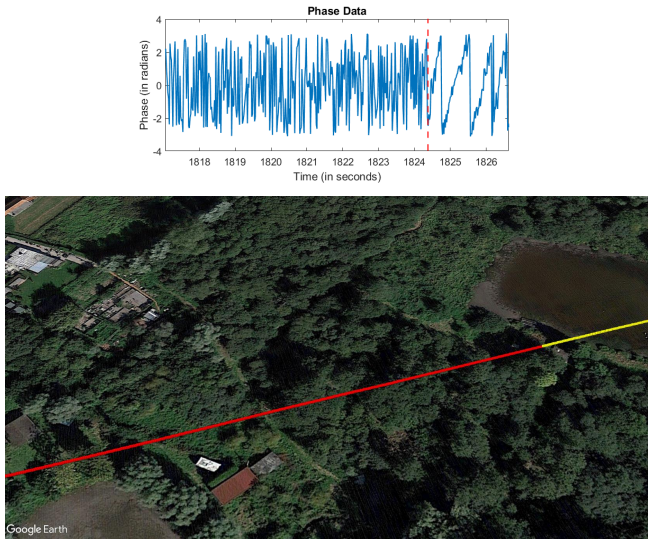

Fig. 4: 10 seconds of phase data from the reflected GNSS signal of GPS satellite PRN 5, representing a rough land surface(in red) in the first segment and a smooth lake surface(in yellow) in the second segment, with the detected change accurately identified.

VI. Conclusion

The proposed methodology employs an offline Bayesian Change-Point Detection approach to identify phase variations in reflected GNSS signals, modeling the phase with a Von Mises distribution. Change points are estimated by minimizing a contrast function derived after parameter estimation via spectral representation of the excess Doppler, leveraging a Bayesian segmentation technique adapted from prior research. The detection process optimizes a penalized contrast function, where the number and positions of changes are determined through empirical likelihood estimation, with a user-defined penalty parameter regulating segmentation sensitivity. The proposed method is evaluated against a classical change detection approach that identifies spectral changes using the Euclidean Distance (ED), with results demonstrating its superior performance. The evaluation is conducted on synthetic GNSS phase data, and the proposed method is further applied to real GNSS-R measurements, accurately detecting changes between different surface characteristics.

References

[1] Yu, K. (2021). Theory and practice of GNSS reflectometry. Berlin/Heidelberg, Germany: Springer.

[2] Anderson, S. G., Wang, Y., Morton, Y. J. (2025). Relating GNSS Reflected Signal Coherence to Ice Shelf Surface Deformation and Roughness. IEEE Transactions on Geoscience and Remote Sensing.

[3] Chamseddine, A., Stienne, G., Reboul, S., Issa, H., Faour, G. (2024, August). Phase Coherence Change Detection via Circular Uniformity Test Applied to GNSS-Reflectometry. In 2024 32nd European Signal Processing Conference (EUSIPCO) (pp. 2367-2371).

[4] Brazier, K. T. S. (1994). Confidence intervals from the Rayleigh test. Monthly Notices of the Royal Astronomical Society, 268(3), 709-712.

[5] Katser, I., Kozitsin, V., Lobachev, V., Maksimov, I. (2021). Unsupervised Offline Changepoint Detection Ensembles. Applied Sciences, 11(9), 4280.

[6] Reboul, S., Benjelloun, M. (2006). Joint segmentation of the wind speed and direction. Signal Processing, 86(4), 744-759.

[7] Barry, D., Hartigan, J. A. (1993). A Bayesian analysis for change point problems. Journal of the American Statistical Association, 88(421), 309-319.

[8] Prexl, J., Saha, S., Zhu, X. X. (2021, July). Mitigating spatial and spectral differences for change detection using super-resolution and unsupervised learning. In 2021 IEEE International Geoscience and Remote Sensing Symposium IGARSS (pp. 3113-3116).

[9] Volpi, M., Camps-Valls, G., Tuia, D. (2015). Spectral alignment of multi-temporal cross-sensor images with automated kernel canonical correlation analysis. ISPRS journal of photogrammetry and remote sensing, 107, 50-63.

[10] Wen, X., Yang, X. (2009, July). Change detection from remote sensing imageries using spectral change vector analysis. In 2009 Asia-Pacific Conference on Information Processing (Vol. 2, pp. 189-192).

[11] O. A. de Carvalho, R. Fontes Guimaraes, R. A. Trancoso Gomes and N. C. da Silva, "Spectral change detection," 2007 IEEE International Geoscience and Remote Sensing Symposium, Barcelona, Spain, 2007, pp. 1935-1938

[12] Chehade, S. E. H., Issa, H., Stienne, G., Reboul, S. (2024). Change Point Detection in Radar Reflectivity Measurements Contaminated by Speckle Noise. IEEE Journal of Selected Topics in Applied Earth Observations and Remote Sensing.

[13] Stienne, G., Reboul, S., Azmani, M., Choquel, J. B., Benjelloun, M. (2014). A multi-temporal multi-sensor circular fusion filter. Information Fusion, 18, 86-100.

[14] Issa, H., Stienne, G., Reboul, S., Raad, M., Faour, G. (2021). Airborne gnss reflectometry for water body detection. Remote Sensing, 14(1), 163.